

Equilibrium electrodeformation of a spheroidal vesicle in an ac electric field

H. Nanguia and Y.-N. Young

Department of Mathematical Sciences, New Jersey Institute of Technology, Newark, New Jersey 07102, USA

(Received 26 August 2013; published 25 November 2013)

In this work, we develop a theoretical model to explain the equilibrium spheroidal deformation of a giant unilamellar vesicle (GUV) under an alternating (ac) electric field. Suspended in a leaky dielectric fluid, the vesicle membrane is modeled as a thin capacitive spheroidal shell. The equilibrium vesicle shape results from the balance between mechanical forces from the viscous fluid, the restoring elastic membrane forces, and the externally imposed electric forces. Our spheroidal model predicts a deformation-dependent transmembrane potential, and is able to capture large deformation of a vesicle under an electric field. A detailed comparison against both experiments and small-deformation (quasispherical) theory showed that the spheroidal model gives better agreement with experiments in terms of the dependence on fluid conductivity ratio, permittivity ratio, vesicle size, electric field strength, and frequency. The spheroidal model also allows for an asymptotic analysis on the crossover frequency where the equilibrium vesicle shape crosses over between prolate and oblate shapes. Comparisons show that the spheroidal model gives better agreement with experimental observations.

DOI: [10.1103/PhysRevE.88.052718](https://doi.org/10.1103/PhysRevE.88.052718)

PACS number(s): 87.50.C-, 47.65.-d, 83.10.-y, 77.84.Nh

I. INTRODUCTION

Biological cells (such as erythrocytes, yeast cells) are found to orient themselves parallel or perpendicular to the direction of an external electric field [1–3], depending on membrane elasticity, coupling between the membrane and the cytoskeleton, excess membrane area, and also solution conductivity [4–6]. Due to the complexity of biological cells, the electrodeformation and electrodynamics of vesicles (closed lipid bilayer membranes) have been intensively pursued as a paradigm for understanding how a biological cell behaves under an electric field. Studies on vesicles also show that they take on different equilibrium shapes depending on the frequency of the imposed alternating current (ac) electric fields and the mismatch in fluid conductivities [7–10]. Changes in vesicle orientation, dielectrophoresis, and electrorotation have also been observed. Under direct current (dc) electric fields, both vesicles and biological cells tend to undergo large deformations with aspect ratios reaching 10. The permeabilization of vesicles membranes by electric fields has also generated a lot of practical and modeling interest, especially in the biotechnology industry. Electroporation, the process of perforating the membrane by applying an (often dc) electric field, has been proposed as a method for delivering molecules into living organisms [11–19]. Most recently, electroporation has been used for measurements of various properties of the cell membranes [19,20].

The earliest theoretical models of vesicle electrodeformation [21,22] were based on minimizing the total surface energy, consisting of the membrane mechanical energy (from tension and bending) and electrical energy (from Maxwell stresses). These models focus on a conductivity ratio ≈ 1 , and as a result the models were only able to predict prolate shape. An extension of these models [23,24] allows for large conductivity mismatch and predicts the various shapes observed experimentally [10], even though poor quantitative agreement with the experiments is found. To our knowledge, Hyuga *et al.* [25,26] proposed the first theory beyond the surface energy-minimization approach. Sadik *et al.* [27] modified this approach to model the deformation of spheroidal vesicles under strong electric fields.

Vlahovska *et al.* [28] proposed a perturbative method to study the dynamics and deformation of a nearly spherical vesicle subject to weak ac electric fields. Assuming small asphericity, the transmembrane potential for a dielectric spherical shell in ac fields is used in their analyses. The small-deformation results are in qualitative agreement with experiments in terms of shape elongation and the transition frequency between prolate and oblate vesicle. Yet the small-deformation model does not apply to vesicles under moderate and strong electric fields, where deformations are well beyond small asphericity [7]. Zhang *et al.* [29] proposed a spheroidal model to study the transient dynamics of highly deformed vesicles under strong dc electric fields. Assuming that vesicles remain spheroidal under a slowly varying dc electric field, which is well supported by experimental findings in [7,27,30], their spheroidal results are in quantitative agreement with experimental data [29] in terms of the vesicle aspect ratio and its response to an electric pulse.

In this work, we extend Zhang *et al.*'s spheroidal model [29] to study the equilibrium electrodeformation of a vesicle in ac fields. Unlike the dynamical approach for solving the transmembrane potential in [29], we develop a model for the equilibrium transmembrane potential for a spheroidal dielectric shell in ac fields. The article is organized as follows: In Sec. II we formulate the problem. In Sec. II A we present the transmembrane potential for a spheroidal dielectric shell; we then derive the governing equation in Sec. II B. Our findings are summarized in Sec. III: We first present a comparison between the spheroidal model and the small-deformation theory for a prolate vesicle; in Sec. III A we consider the dependence of vesicle deformation, transmembrane potential, and electric stresses on the field frequency. In Sec. III B we show the predictions, as well as comparison with experiment for the shape elongation and transition frequency.

II. PROBLEM FORMULATION

Figure 1 illustrates a spheroidal vesicle enclosing an interior dielectric fluid ($\mu_i, \epsilon_i, \sigma_i$) suspended in another dielectric

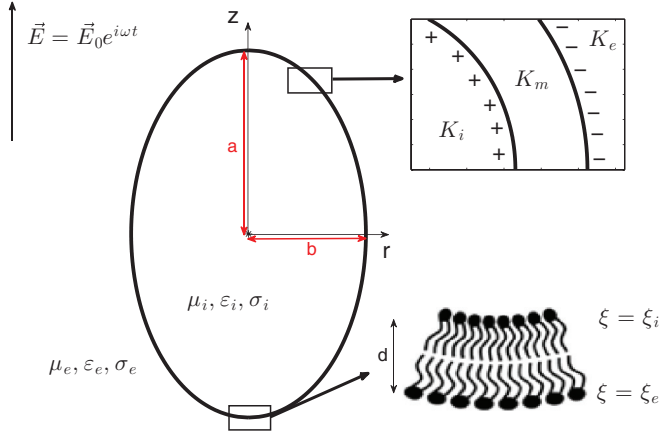


FIG. 1. (Color online) Illustration of a vesicle suspended in a leaky dielectric fluid. The typical membrane thickness is $d = 5$ nm. The bottom inset shows the lipid bilayer structure of the membrane, and the top inset shows the three dielectric spheroidal shells with electric impedance defined in Eq. (9).

fluid with $(\mu_e, \varepsilon_e, \sigma_e)$. μ , ε , and σ are the fluid viscosity, dielectric permittivity, and conductivity, respectively, and the subscript denotes interior (i) or exterior (e) fluids. Typical values of the fluid viscosity (larger than 10^{-3} Pa s) and vesicle size (several μm 's) indicate that the fluid inertia are negligible, consequently the flow velocity in both interior and exterior fluids is governed by the incompressible Stokes equations

$$\mu_j \nabla^2 \mathbf{u}_j = \nabla p_j, \quad \nabla \cdot \mathbf{u}_j = 0, \quad (1)$$

where p is the fluid pressure and \mathbf{u} is the fluid velocity, with the subscript $j = e$ for exterior fluid or $j = i$ for interior fluid. The boundary conditions for the velocity are $\mathbf{u} = \mathbf{0}$ in the far-field and $\mathbf{u} = \frac{dx}{dt}$ on the vesicle membrane, with \mathbf{x} denoting the vesicle membrane location. The balance of stresses on the membrane gives

$$\mathbf{n} \cdot [\mathbf{T} + \mathbf{S}] = \boldsymbol{\tau}^{\text{mem}}, \quad (2)$$

where $[[f]] \equiv f_e - f_i$ denotes the difference between exterior and interior and \mathbf{n} is the outward normal unit vector on the membrane. $\mathbf{T} = -p\mathbf{I} + \mu[(\nabla\mathbf{u})^T + \nabla\mathbf{u}]$ is the hydrodynamic stress with \mathbf{I} the identity tensor, and $\mathbf{S} = \varepsilon\vec{\mathbf{E}}\vec{\mathbf{E}} - \frac{\varepsilon}{2}(\vec{\mathbf{E}} \cdot \vec{\mathbf{E}})\mathbf{I}$ is the Maxwell stress tensor. The membrane traction consists of membrane tension and bending forces,

$$\boldsymbol{\tau}^{\text{mem}} = 2\sigma_h H \mathbf{n} - \kappa (4H^3 - 4KH + 2\nabla_s^2 H) \mathbf{n}, \quad (3)$$

where σ_h , κ , H , and K are the membrane tension, bending rigidity, mean curvature, and Gaussian curvature, respectively. The (homogeneous) membrane tension is related to the excess area $\Delta \equiv \frac{A}{4\pi r_0^2} - 1$ as

$$\sigma_h = s_0 \exp \left[\frac{8\pi\kappa\Delta}{k_B T} \right], \quad (4)$$

where $s_0 = \sigma_0/(\kappa/r_0^2)$ is the dimensionless membrane tension.

The electric field is harmonic ($\vec{\mathbf{E}} = \vec{\mathbf{E}}_0 e^{i\omega t}$) and irrotational, which implies that $\vec{\mathbf{E}} = -\nabla\phi$ with ϕ the electric potential that satisfies the Laplace equation both inside and outside the

vesicle,

$$\nabla^2 \phi_j = 0. \quad (5)$$

Across the membrane, the electric potential has a jump

$$\phi_i - \phi_e = \Delta\phi, \quad (6)$$

due to the capacitive nature of the vesicle membrane. The induced charges on the two sides of the membrane cause a discontinuity in the displacement vector,

$$[[\varepsilon\vec{\mathbf{E}} \cdot \mathbf{n}]] = Q(\omega, t), \quad (7)$$

where Q is the induced charge density. If we neglect the effects of charge convection along the membrane, the electric current conservation at the interface gives

$$[[\sigma\vec{\mathbf{E}} \cdot \mathbf{n}]] = -\frac{dQ}{dt} \approx -\frac{\partial Q}{\partial t}. \quad (8)$$

Substituting Eq. (7) into Eq. (8) yields the continuity condition

$$[-K\nabla\phi \cdot \mathbf{n}] = 0, \quad K_j = \sigma_j + i\omega\varepsilon_j, \quad (9)$$

where the dielectric properties are characterized by the complex electrical impedance. j can be i , m , and e , referring to the interior, membrane, and exterior of the vesicle. σ_j , ε_j , and ω are the conductivity, permittivity, and electric field frequency, respectively. For the vesicle's impedance, $K_m = G_m d + iC_m d$, where G_m and C_m are the membrane conductance and capacitance.

The governing equations are nondimensionalized by scaling length to r_0 , time to the charging time $t_c = \varepsilon_e/\sigma_e$, the electric potential to $E_0 r_0$, bending force and membrane tension to κ/r_0^2 , and electric stresses to $\varepsilon_e E_0^2$. For example, the resultant dimensionless complex conductivities are given by

$$K_e = \frac{1}{x} + i\frac{\omega}{x}, \quad K_i = \frac{\sigma_r}{x} + i\frac{\omega\varepsilon_r}{x}, \quad K_m = \frac{\sigma_m}{\sigma_e x} + i\omega\frac{\varepsilon_m}{\varepsilon_e x}, \quad (10)$$

where the conductivity and permittivity ratios are defined as $\sigma_r = \frac{\sigma_i}{\sigma_e}$ and $\varepsilon_r = \frac{\varepsilon_i}{\varepsilon_e}$. $x = \frac{d}{r_0}$ is the dimensionless thickness. σ_m and ε_m are the membrane conductivity and permittivity, respectively.

A. Transmembrane potential

In the leaky dielectric framework, cations and anions in the bulk are assumed to neutralize instantaneously, while net surface charge can be induced on the interface between fluids of mismatched dielectric conductivity and/or permittivity. Because the membrane is impermeable, the induced surface charges accumulate on either side of the membrane, giving rise to a transmembrane potential across the membrane. In the past studies of vesicles subjected to ac electric fields [28,31], the transmembrane potential for a spherical shell was often used [32–34]. However, the transmembrane potential depends on the geometry of the vesicle, and even small deviations from an initial spherical shape may induce noticeable changes in the potential jump [35].

Analytical studies on the induced transmembrane potential for spheroidal vesicles reveal that the membrane thickness is nonuniform due to the alignment of cell boundaries with

spheroidal surfaces [36,37]. Klee and Plonsey [38] used numerical simulations to compute the spheroidal potential jump, while Gimsa *et al.* [35,39,40] devised a resistor-capacitor (RC) approach to determine the induced transmembrane potential. Later, Konik [41] showed that small variations in the membrane thickness of spheroidal cells have no effects on the transmembrane potential.

Here we developed an analytical model of the transmembrane potential for a spheroidal shell in an ac electric field. The analytical solution is based on the truncated expansion in Gegenbauer functions for the electric potential in the prolate spheroidal coordinates (ξ, η) , which are related to the cylindrical coordinates (r, z) as

$$z = c\xi\eta, \quad r = c\sqrt{(\xi^2 - 1)(1 - \eta^2)}, \quad (11)$$

where $c \equiv \sqrt{b^2 - a^2}$ is the semifocal length. Surfaces of constant $\xi \in [1, \infty)$ are spheroids while surfaces of constant $\eta \in [-1, 1]$ are hyperboloids. As such, the prolate vesicle surface is given by $\xi = \xi_0(t) \equiv \frac{a}{c}$.

The electric potential exists in three domains: interior (*i*), exterior (*e*), and the membrane (*m*); see the inset in Fig. 1. The transmembrane potential is derived by solving Laplace equations in all three domains as follows. We first assume that the potential in each domain takes the truncated form [29,42–44]

$$\phi_j = [\alpha_j \xi + \beta_j Q_1(\xi)]\eta, \quad j = i, e, m, \quad (12)$$

where Q_1 is the Legendre polynomial of the second kind. α_j and β_j are obtained from the boundary conditions. For example, $\alpha_e = -c$ and $\beta_i = 0$ from the far-field and interior boundary conditions. The remaining coefficients $\beta_e, \alpha_m, \beta_m$, and α_i are determined from boundary conditions on the membrane; see Appendix B. Substituting the coefficients in Eq. (12), we obtain the transmembrane potential

$$\Delta\phi = \phi_i(\xi_i) - \phi_e(\xi_e) \equiv V_m \eta,$$

where $V_m = cF(\omega)/D(\omega)$ is the ‘‘amplitude’’ of the potential, $D(\omega)$ is given by Eq. (B7), and

$$F(\omega) = -K_e(Q_e - \xi_e Q'_e)[(K_i - K_m)\xi_i Q_e + (-K_i \xi_e + K_m \xi_i)Q_i + K_m(\xi_e - \xi_i)\xi_i Q'_i]. \quad (13)$$

The functions $Q_e \equiv Q_1(\xi_e)$, $Q_i \equiv Q_1(\xi_i)$, $Q'_e \equiv Q'_1(\xi_e)$, $Q'_i \equiv Q'_1(\xi_i)$.

Figure 2 provides a comparison of the transmembrane potential magnitude V_m between the spherical shell (dashed lines) and spheroidal shells (dash-dotted lines). Thick lines are for prolate with $\sigma_r = 1.5$, and thin lines are for oblate with $\sigma_r = 0.5$. At low frequencies, the spherical shell potential reaches the maximum value $V_m = 3/2$ while for the spheroidal shell V_m plateaus to a maximum that depends on the vesicle aspect ratio a/b : The larger the shape elongation, the larger the maximum transmembrane potential, in agreement with earlier findings about the dependence of the potential on shape [35]. We note that by solving the Laplace equation in each dielectric spheroidal shell, the η dependence in our spheroidal shell is the same as that in the spherical shell, while Gimsa *et al.*'s model cannot capture the η dependence.

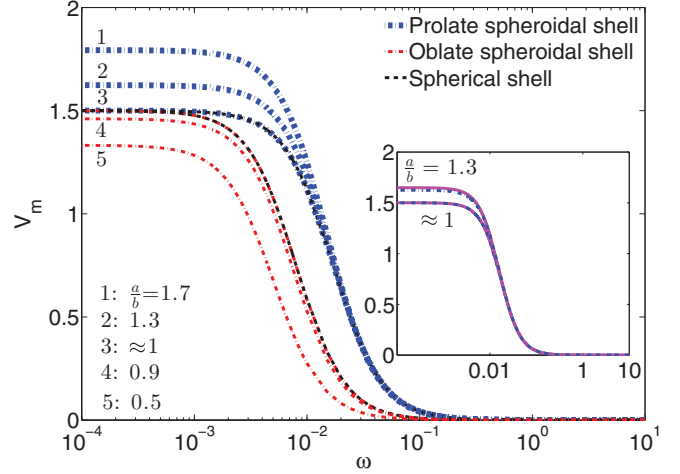


FIG. 2. (Color online) Magnitude of transmembrane potential calculated from Eq. (13) for various aspect ratios. The thick (thin) dash-dotted lines are prolate, $\sigma_r = 1.5$ (oblate, $\sigma_r = 0.5$) predictions, and the dashed line is the spherical shell potential. The inset shows V_m for two prolate cases.

B. Electrohydrodynamic deformation

With the transmembrane potential for the spheroidal shell in Eq. (13), we can now compute the electric potentials in the interior and exterior of the vesicle as

$$\phi_e = [-c\xi + \alpha Q_1(\xi)]\eta e^{i\omega t}, \quad (14)$$

$$\phi_i = \beta\xi\eta e^{i\omega t}, \quad (15)$$

where α and β are obtained by satisfying the boundary conditions in Eqs. (6) and (9):

$$\alpha = \frac{c\xi_0(K_r - 1) - K_r V_m}{K_r Q_1 - \xi_0 Q'_1}, \quad \beta = \frac{c(\xi_0 Q'_1 - Q_1) - V_m Q'_1}{K_r Q_1 - \xi_0 Q'_1}, \quad (16)$$

with $K_r = \frac{K_i}{K_e}$. We write the electric field \vec{E} as the real part of \mathcal{E} : $\vec{E} = \frac{1}{2}(\vec{\mathcal{E}} + \vec{\mathcal{E}}^*)$ (where the asterisk denotes complex conjugation), and substitute it into the Maxwell stress [45],

$$\mathbf{S}(\omega) = \frac{\varepsilon}{4}(\vec{\mathcal{E}}\vec{\mathcal{E}}^* + \vec{\mathcal{E}}^*\vec{\mathcal{E}} - |\mathcal{E}|^2\mathbf{I}) + \frac{\varepsilon}{4}\left(\vec{\mathcal{E}}\vec{\mathcal{E}} + \vec{\mathcal{E}}^*\vec{\mathcal{E}}^* - \frac{1}{2}[\vec{\mathcal{E}} \cdot \vec{\mathcal{E}} + \vec{\mathcal{E}}^* \cdot \vec{\mathcal{E}}^*]\mathbf{I}\right). \quad (17)$$

In the above equation, the first group on the right-hand side is the time-averaged Maxwell stress tensor, and the second group is the time-dependent (harmonic) terms. In the following, we consider only the time-independent terms for equilibrium vesicle shapes.

We focus on the axisymmetric incompressible fluid velocity field, which can be computed from a stream function ψ for both inside and outside the vesicle. The stream function satisfies the equation

$$(E^2)^2\psi = 0, \quad \text{with} \quad E^2 = \frac{1}{c^2(\xi^2 - \eta^2)}\left[(\xi^2 - 1)\frac{\partial^2}{\partial \xi^2} + (1 - \eta^2)\frac{\partial^2}{\partial \eta^2}\right]. \quad (18)$$

The general solution for the stream function takes the form [46,47]

$$\psi = g_0(\xi)G_0(\eta) + \sum_{n=2}^{\infty} [g_n(\xi)G_n(\eta) + h_n(\xi)H_n(\eta)], \quad (19)$$

where G_n and H_n are the Gegenbauer functions of the first and second kind, respectively. Detailed expressions of the functions g_n and h_n can be found in [46,47]. In this work, we seek a truncated solution [29,42–44]

$$\psi_e = [A_3^1 H_1(\xi) + A_3^3 H_3(\xi)] G_3(\eta), \quad (20)$$

$$\psi_i = [B_3^3 G_3(\xi) + B_3^5 G_5(\xi)] G_3(\eta). \quad (21)$$

Four boundary conditions are needed to determine the four coefficients A_3^1 , A_3^3 , B_3^3 , and B_3^5 . Following the procedures in [29,48], we project the stress balance onto the corresponding velocities to close the system:

$$\int_{\xi=\xi_0(t)} u[\mathbf{T}_{\xi\eta}] + [\mathbf{S}_{\xi\eta}] ds = 0, \quad (22)$$

$$\int_{\xi=\xi_0(t)} v[\mathbf{T}_{\xi\xi}] + [\mathbf{S}_{\xi\xi}] - \tau^{\text{mem}} ds = 0, \quad (23)$$

where $\tau^{\text{mem}} = \boldsymbol{\tau}^{\text{mem}} \cdot \mathbf{n}$. In prolate spheroidal coordinates,

$$\mathbf{T}_{\xi\xi} = 2\mu \left(\frac{\partial v}{h_\xi \partial \xi} + \frac{u}{h_\xi h_\eta} \frac{\partial h_\xi}{\partial \eta} \right), \quad (24)$$

$$\mathbf{T}_{\xi\eta} = \mu \left(\frac{\partial(u/h_\eta)}{\partial \xi} \frac{h_\eta}{h_\xi} + \frac{\partial(v/h_\xi)}{\partial \eta} \frac{h_\xi}{h_\eta} \right),$$

$$\mathbf{S}_{\xi\xi} = \frac{\varepsilon}{4} (\mathcal{E}_\xi \mathcal{E}_\xi^* - \mathcal{E}_\eta \mathcal{E}_\eta^*), \quad \mathbf{S}_{\xi\eta} = \frac{\varepsilon}{4} (\mathcal{E}_\xi \mathcal{E}_\eta^* + \mathcal{E}_\eta \mathcal{E}_\xi^*), \quad (25)$$

where h_ξ and h_η are the scale factors in the spheroidal coordinates, and $\mathcal{E}_\xi = -\frac{\partial\phi}{h_\xi \partial \xi}$ and $\mathcal{E}_\eta = -\frac{\partial\phi}{h_\eta \partial \eta}$ are the normal and tangential electric field. The excess area in Eq. (4) can be expressed in terms of ξ_0 as

$$\Delta = \frac{1}{2} (1 - \xi_0^{-2})^{-2/3} \left[1 - \xi_0^{-2} + \sqrt{\xi_0^2 - 1} \arcsin(\xi_0^{-1}) \right] - 1. \quad (26)$$

The above derivation can be modified for the oblate case with appropriate transformation: $\xi \rightarrow i\lambda$ and $c \rightarrow -i\bar{c}$, with i the imaginary unit. Thus the oblate spheroidal coordinates (λ, η) are related to the cylindrical coordinates (r, z) as $z = \bar{c}\lambda\eta$, $r = \sqrt{(\lambda^2 + 1)(1 - \eta^2)}$, with $\bar{c} \equiv \sqrt{b^2 - a^2}$ for $\lambda \in [0, \infty)$ and $\eta \in [-1, 1]$. Surfaces of constant λ are oblate spheroids while surfaces of constant η are hyperboloids. Consequently, in oblate coordinates,

$$E^2 = \frac{1}{\bar{c}^2(\lambda^2 + \eta^2)} \left[(\lambda^2 + 1) \frac{\partial^2}{\partial \lambda^2} + (1 - \eta^2) \frac{\partial^2}{\partial \eta^2} \right],$$

the electric potential coefficients and excess area take the following forms:

$$\alpha = \frac{\bar{c}\lambda_0(K_r - 1) - K_r V_m}{K_r Q_1 - \lambda_0 Q_1'}, \quad (27)$$

$$\beta = i \frac{[\bar{c}Q_1 + (V_m - c\lambda_0)Q_1']}{K_r Q_1 - \lambda_0 Q_1'}$$

$$\Delta = \frac{1}{2} (1 + \lambda_0^{-2})^{-2/3} \left[\sqrt{\lambda_0^{-2} + \lambda_0^{-4}} + \operatorname{arctanh}[(\lambda_0^2 + 1)^{-1/2}] \right] - 1. \quad (28)$$

Coefficients A_3^1 , A_3^3 , B_3^3 , and B_3^5 are expressed in terms of χ (with $\chi = \xi_0$ for prolate and λ_0 for oblate) through stress balance [Eqs. (22) and (23)] and velocity continuity on the membrane; for details of the derivation, see [29]. To close the system, we use the kinematic condition at the membrane, which gives the normal velocity in terms of χ , and we finally obtain the governing equation for the shape function as

$$\frac{d\chi}{dt} = \frac{\delta[\mathcal{Q}_N f_{21} + \mathcal{Q}_T \frac{f_{11}(\mu_r f_{22} + f_{23})}{\mu_r f_{14} + f_{15}} - \text{Ca}_E^{-1}(\sigma_h f_{24} + f_\kappa)]}{\frac{2}{3}(\mu_r f_{25} + f_{26})}, \quad (29)$$

$$\mathcal{Q}_N = \pm \frac{1}{2c^2} [2c^2 - 2c\tau_3(Q_1' + Q_1/\chi) + (\tau_3^2 + \tau_4^2)[Q_1'^2 + (Q_1/\chi)^2] - 2(\tau_1^2 + \tau_2^2)/\varepsilon_r], \quad (30)$$

$$\mathcal{Q}_T = \frac{1}{2c^2} [c^2\chi + (\tau_3^2 + \tau_4^2)Q_1 Q_1' - c\tau_3(Q_1 + \chi Q_1') - (\tau_1^2 + \tau_2^2)\chi/\varepsilon_r], \quad (31)$$

where the symbols \pm designate prolate (+) or oblate (−). $\text{Ca}_E = \frac{\varepsilon_e t_0^3 E_0^2}{\kappa}$ is the electric capillary number, and $\delta = \frac{t_c}{t_{\text{EHD}}}$, with $t_{\text{EHD}} = \frac{\mu_i}{\varepsilon_e E_0^2}$ the characteristic electrohydrodynamics (EHD) time scale. The functions f_{11} – f_{26} , f_κ are given by Eqs. (A1)–(A11) for the prolate shape and Eqs. (A13)–(A23) for the oblate shape. Setting $\frac{d\chi}{dt} = 0$, the steady-state equilibrium shape is obtained by solving the nonlinear equation,

$$\mathcal{Q}_N f_{21} + \mathcal{Q}_T \frac{f_{11}(\mu_r f_{22} + f_{23})}{\mu_r f_{14} + f_{15}} = \text{Ca}_E^{-1}(\sigma_h f_{24} + f_\kappa). \quad (32)$$

Equation (32) shows that an equilibrium shape is achieved when the electric forces (on the left) are balanced by the tension and bending forces (on the right). The viscous effects are manifested in terms that involve the viscosity ratio μ_r .

III. RESULTS

A. Comparison with small-deformation theory

The shape elongation $a/b = \xi_0/\sqrt{\xi_0^2 - 1}$ for prolate while $a/b = \lambda_0/\sqrt{\lambda_0^2 + 1}$ for oblate. Figure 3(a) shows the equilibrium shape elongation from the spheroidal model (solid lines) and the small-deformation theory [28] (dashed lines) for $\sigma_r = 1.5$, $\text{Ca}_E = 6837$ and $s_0 = 1$ (figures 6 and 7 in [28]). We found that, for the same membrane tension s_0 , the spheroidal model predicts larger deformation than the small deformation theory at a given frequency. The corresponding transmembrane potential magnitude V_m and the electric stresses (the normal component Q_N and the tangential component Q_T) are shown

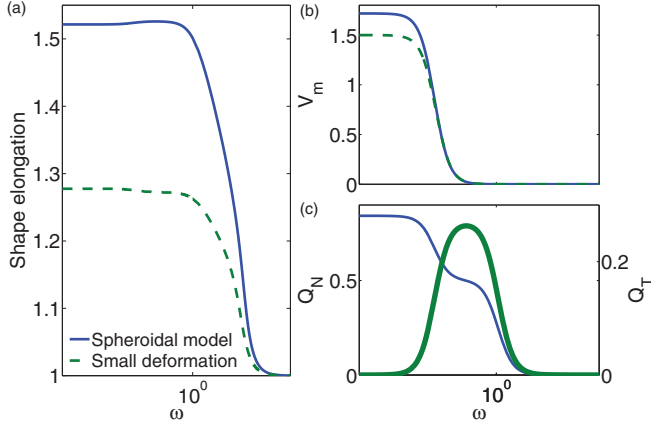


FIG. 3. (Color online) Equilibrium deformation vs frequency ω for a prolate vesicle with $\sigma_r = 1.5$, $Ca_E = 6837$, and $s_0 = 1$. In (a) and (b), solid curves are from the spheroidal model and dashed curves are from the small-deformation model. (c) Normal (thin curve) and tangential (thick curve) electric stresses from the spheroidal model [Eqs. (30) and (31)].

in Figs. 3(b) and 3(c), respectively. As we expect from Sec. II A, the membrane potential from the spheroidal model is higher at low frequencies. The decrease in membrane potential at $\omega \approx 5 \times 10^{-3}$ in (b) coincides with an increase in the tangential electric stress and a decrease in the electric pressure in (c).

B. Comparison with experiment

1. Equilibrium shape elongation versus frequency

Experiments [10] show that the vesicle takes a spherical shape at equilibrium under very high frequencies ($\omega > 10^3$) when the transmembrane potential is zero. At moderate frequencies ($\omega < 10^2$), the equilibrium vesicle shape can be prolate (for $\sigma_r > 1$) or oblate (for $\sigma_r < 1$). In particular, the equilibrium oblate vesicle for $\sigma_r < 1$ crosses over to the prolate equilibrium shape at low frequencies, $\omega < 10^{-2}$. These experimental findings are summarized (symbols) in Figs. 4 and 5, where we also compare the spheroidal model (solid lines) and the small-deformation model [28] (broken lines).

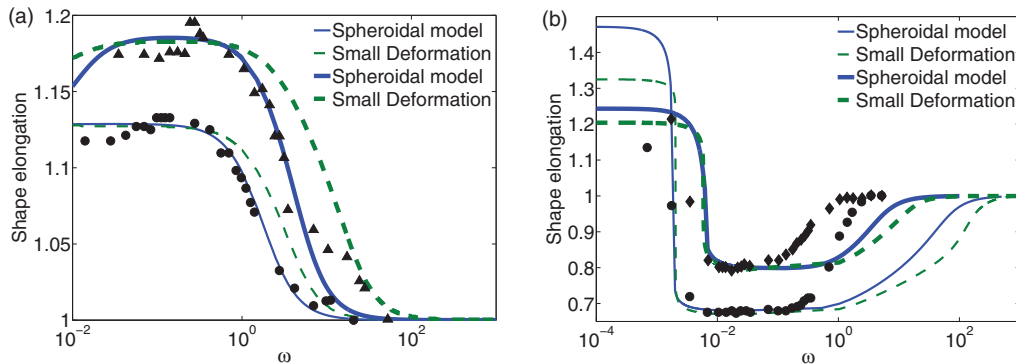


FIG. 4. (Color online) Comparison between the experimental data of Aranda *et al.* [10] (symbols), the small-deformation theory (dashed curves), and the current model (solid curves). (a) $\sigma_r > 1$, (b) $\sigma_r < 1$.

TABLE I. Fitted values of $s_0 = \bar{\sigma}_0 r_0^2 / \kappa$ for the experimental data in [10] with $\epsilon_r = 1$, $\mu_r = 1$, $\kappa = 10k_B T$, and $E_0 = 0.2$ kV/cm.

Experiment	s_0 used in spheroidal model	s_0 used in small-deformation model
$\sigma_r = 4.3$, $r_0 = 21.6 \mu\text{m}$	43 000	3000
$\sigma_r = 1.7$, $r_0 = 27.5 \mu\text{m}$	80 000	20 000
$\sigma_r \approx 1$ (Pr), $r_0 = 27.5 \mu\text{m}$	1000	1
$\sigma_r \approx 1$ (Ob), $r_0 = 37.5 \mu\text{m}$	10^{-6}	10^{-7}
$\sigma_r = 0.5$, $r_0 = 12.8 \mu\text{m}$	1000	100
$\sigma_r = 0.4$, $r_0 = 27.2 \mu\text{m}$	70	1

Following the approach in [28], we use s_0 as a fitting parameter (see Table I) and fix the bending stiffness $\kappa = 10k_B T$. We note that s_0 used in the spheroidal model is at least an order of magnitude larger than in small deformation. Nevertheless, they are comparable to values reported in previous work [30].

Figure 4(a) is for $\sigma_r > 1$ [“transition” (1) in [10]] where the equilibrium shape elongation is always greater than (prolate) or equal to (spherical) 1. We observe better agreement from the spheroidal model for $\sigma_r = 1.7$, while for $\sigma_r = 4.3$ the spheroidal results are in better agreement except for $\omega > 10$. Figure 4(b) is for $\sigma_r < 1$ [“transition” (4) in [10]], where the equilibrium shape can cross over from spherical at high frequencies $\omega > 20$ to oblate at intermediate frequencies $\sim 3 \times 10^{-3} \leq \omega \leq \sim 1$, and to prolate at low frequencies $10^{-4} \leq \omega \leq \sim 3 \times 10^{-3}$. In this case, neither model agrees with the experiments for $1 > \omega > 0.5$, where the equilibrium vesicle shape crosses over from oblate to spherical as ω increases.

In “transition” (3) of [10], where σ_r is close to unity, the value of σ_r determines the shape of the vesicles: prolate for $\sigma_r > 1$ and oblate for $\sigma_r < 1$. Figure 5(a) shows the comparison between models and experiments for $\sigma_r \approx 1$. Next we focus on the effect of bending rigidity on the equilibrium vesicle shape. For experiments in [10], the bending stiffness varies between 4×10^{-20} J [30] and 2.3×10^{-19} J [49]. Recent measurements on SOPC bilayer membranes [50] reported a bending stiffness as low as 7×10^{-21} J. Figure 5(b) shows a comparison between theories and

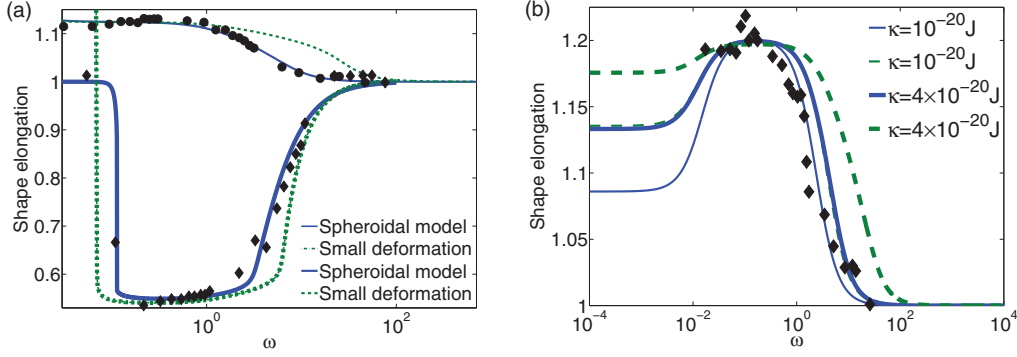


FIG. 5. (Color online) Comparison between the experimental data of Aranda *et al.* [10] (symbols), the small-deformation theory (dashed curves), and the spheroidal model (solid curve). (a) $\sigma_r \approx 1$, (b) $\sigma_r = 4.5$.

experiments for $\sigma_r = 4.5$ and with various values of the bending stiffness. Both theories are very sensitive to changes in the bending stiffness: We found good agreement with experiments up to $\kappa = 4 \times 10^{-20}$ J for the spheroidal model and up to $\kappa = 10^{-20}$ J for the small deformation. Beyond these values, the two models overestimate the deformation.

Vesicles take various equilibrium shapes at different frequencies and conductivity ratios. Aranda *et al.* [10] constructed a morphological diagram on the ω - σ_r plane by performing a series of experiments using over 60 vesicles ranging from 4 to 50 μm in size. They subjected all these vesicles to an ac field at a frequency ranging between ≈ 2 kHz and 20 MHz while varying the conductivity of the external fluid phase with fixed conductivity inside the vesicles.

Figure 6 shows the shape variations in the ω - σ_r plane. The experimental data points indicate the value at which the vesicle changes shape as frequency increases. Figure 6 also compares the predictions from the spheroidal model, the small-deformation theory, and the result using the energy-minimization approach [23]. The spheroidal and small-deformation models give agreement with experiments: The prolate-to-oblate and prolate-to-sphere frequencies increase with σ_r , while the oblate-to-sphere frequencies decrease with increasing σ_r . The surface energy-minimization model in [23] (starred-solid lines) only gives qualitative agreement with experiments.

2. Prolate-to-oblate crossover frequency

The frequency at which the equilibrium vesicle shape crosses over from prolate to oblate depends on the conductivity ratio and vesicles size [10,23,51–53]. In a recent experiment, Peterlin [23] put vesicles of different sizes under a sequence of stepwise frequency changes, ranging from hundreds to a thousand hertz for a duration of ≈ 3 s with the frequency increasing or decreasing around the crossover frequency; see the symbols in Fig. 7(a).

At the crossover frequency (from prolate to oblate, for example), the equilibrium vesicle shape is spherical, which corresponds to the limit $\xi_0 \rightarrow \infty$. In this limit, the membrane excess area $\Delta \approx 0$, and V_m reduces to the spherical shell potential. This allows us to perform an asymptotic analysis

on the equilibrium vesicle shape elongation near the crossover frequency, where we expand all functions of ξ_0 in terms of $\xi_0 \sim 1/\epsilon^2$ with $\epsilon \ll 1$. For example, the Legendre polynomial $Q_1(\xi_0)$ and its derivative take the form $Q_1 \sim \frac{1}{3\xi_0^2} + \frac{1}{5\xi_0^4} + O(\frac{1}{\xi_0^6})$, $Q_1' \sim -\frac{2}{3\xi_0^3} - \frac{4}{5\xi_0^5} + O(\frac{1}{\xi_0^7})$. We expand the semifocal length $c \sim \frac{1}{\xi_0} + O(\frac{1}{\xi_0^3})$, and similarly for all the other functions in Appendix A. We then substitute these expansions into Eqs. (16), (30), and (32), and obtain a series expanded in ξ_0^{-2} : $\sum_{n=0} a_n \xi_0^{-2n} = 0$, where the coefficients a_n are functions of fluid and membrane properties. Keeping all the leading-order terms at $O(1/\xi_0^2)$, we obtain an equation for ξ_0^2 , which gives the solution

$$\xi_0(\omega) = \sqrt{\frac{2}{35} \frac{\sqrt{-\text{Ca}_E A B C}}{G}} \quad (33)$$

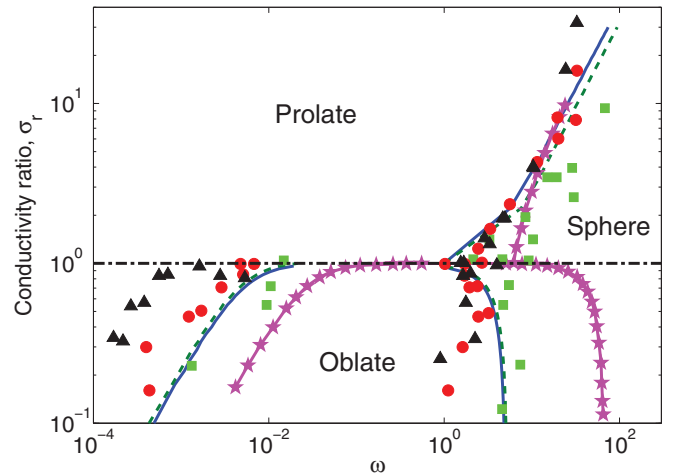


FIG. 6. (Color online) Morphological phase diagram for $\kappa = 10k_B T$, $E_0 = 2 \times 10^4$ V/m. The conductivity ratio σ_r is determined by varying the conductivity of the external medium (σ_e) and holding the interior fixed at $\sigma_i = 15 \mu\text{S}/\text{cm}$ (\square), $65 \mu\text{S}/\text{cm}$ (\circ), $130 \mu\text{S}/\text{cm}$ (\triangle). Solid lines are from the spheroidal model with $s_0 = 45000$, dashed lines are from the small-deformation model with $s_0 = 10000$, and starred-solid lines are from the energy minimization approach [23].

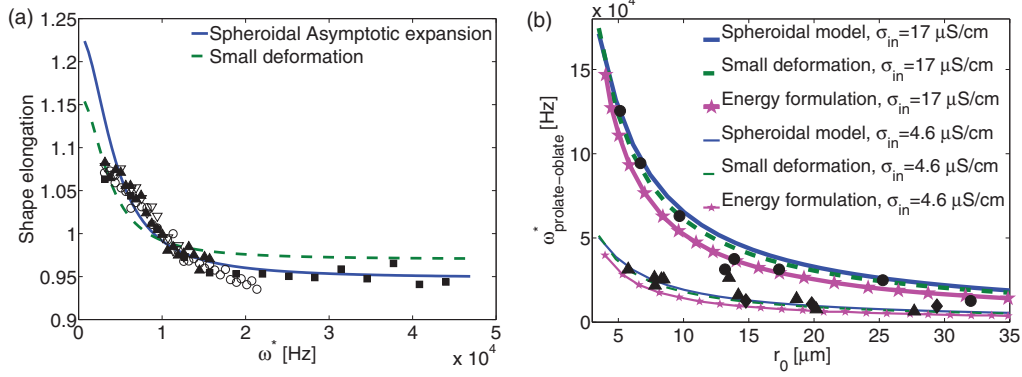


FIG. 7. (Color online) (a) Shape elongation near the crossover between prolate and oblate for $\sigma_r = 0.9$, $d = 4$ nm, $\kappa = 1.2 \times 10^{-19}$ J, and $E_0 = 500$ V/m. Symbols are the experimental data in [23]: Full (open) symbols are with increasing (decreasing) frequency. $s_0 = 1$ is used in both spheroidal and small-deformation models. (b) Prolate-oblate crossover frequency, ω^* , as a function of vesicle radius r_0 .

with coefficients A , B , C , and G given in Appendix D. The leading-order shape elongation for a prolate vesicle near the crossover frequency is $\frac{a}{b} \sim 1 + \frac{1}{2\xi_0^2} + O(\frac{1}{\xi_0^4})$. Similarly for the crossover from oblate to prolate, the leading-order shape elongation would be $\frac{a}{b} \sim 1 - \frac{1}{2\lambda_0^2} + O(\frac{1}{\lambda_0^4})$.

Figure 7(a) shows the comparison between the asymptotic analysis on the spheroidal model (solid line), calculation from the small-deformation model (dashed line), and experiments (symbols). First of all, we observe a small difference in the crossover frequency (value of ω^* when shape elongation is unity) between the solid and the dashed lines: We attribute this small disagreement to the differences in treating the stress balance on the membrane between the two models. Secondly, we observe a significant difference in the slope at the crossover frequency between the two curves, with the spheroidal model in better agreement with the experimental data. We have tried to adjust s_0 to fit the small-deformation model to experimental data with the same slope at the crossover frequency, but we are unable to find a reasonably good fit.

The crossover frequency also depends on the initial spherical size of the vesicles. Figure 7(b) shows the comparison results of the experiment in [23], where the spheroidal results (solid curves), the small-deformation results (dashed curves), and the energy-minimization results (starred solid curves) are all plotted against the initial spherical radius r_0 . All three theories show good agreement with the experimental data.

IV. CONCLUSION

In this work, we constructed a spheroidal model to study the equilibrium deformation of a vesicle under ac electric fields within the leaky dielectric framework. Such an approach has been shown to capture large equilibrium electrodeformation of a viscous surfactant-covered drop [44] and the transient dynamics of a vesicle in a dc field [29]. In our spheroidal model, the vesicle membrane is modeled as a nonconducting capacitive elastic membrane with a homogeneous tension that depends on the excess area. We developed a spheroidal shell model to compute the potential across the vesicle membrane. By adjusting the membrane tension coefficient s_0 , we are able to reproduce the experiments in terms of the dependence of

the vesicle shape elongation on the frequency ω , conductivity ratio σ_r , and the initial spherical radius of the vesicle. We further explore the effects of bending rigidity on the shape elongation. In addition, we conducted an asymptotic analysis on our spheroidal model around the prolate-oblate crossover frequency, and we find very good agreement with the experiments in terms of both the value of the crossover frequency and the rate of change of shape elongation with respect to frequency.

In this work, we did not consider the effects of membrane conductance and displacement currents across the membrane, both of which are found to destabilize a planar membrane under electric fields [54–56]. We focus on the equilibrium deformation and ignore the time-dependent harmonic stresses. Consequently, we did not consider the dynamic transient and oscillation around the averaged equilibria, yet our spheroidal model can easily incorporate the time-dependent stresses, and this is now part of an ongoing work. In addition, the vesicle area is not held constant in our model. Furthermore, our spheroidal model is applicable only to spheroidal deformation, and cannot describe the dynamics and equilibrium shapes of an axisymmetric nonspheroidal vesicle.

We are now refining our model by replacing the leaky dielectric fluids with electrolytes in the solvents, in which case the electric potential no longer satisfies the simple Laplace equation, but rather the Poisson-Boltzmann equations that take into account the transport of various charged species in the fluids. The solvents are known to destabilize lipid membrane under a dc electric field [57]. It is reasonable to expect more complex dynamics and equilibrium shapes for a vesicle immersed in electrolytes under an ac field. For example, a vesicle under an electric field may have very different morphology that depends on the net charges in the bulk. We are currently conducting a numerical investigation into how the morphological phase diagram in Fig. 6 may be altered by solvent electrokinetics.

ACKNOWLEDGMENTS

Y.N.Y. acknowledges useful discussions with P. M. Vlahovska and C. Liu, and partial support from NSF Grant No. DMS-1222550.

APPENDIX A: INTEGRALS IN THE SPHEROIDAL MODEL

In the following equations $N \equiv G_3(\xi_0)G'_5(\xi_0) - G'_3(\xi_0)G_5(\xi_0)$ for prolate, and $N \equiv G_3(\lambda_0)G'_5(\lambda_0) - G'_3(\lambda_0)G_5(\lambda_0)$ for oblate. The functions $f_{11}(\xi_0)$ – $f_{15}(\xi_0)$ are given by

$$f_{11} = \int \frac{\eta G_3(\eta)}{\xi_0^2 - \eta^2} d\eta, \tag{A1}$$

$$f_{12} = \frac{1}{\xi_0^2 - 1} \int G_3(\eta) \left(\frac{2\eta G'_3(\eta)}{(\xi_0^2 - \eta^2)^2} + \frac{G''_3(\eta)}{\xi_0^2 - \eta^2} \right) d\eta, \tag{A2}$$

$$f_{13} = \frac{G'_3 G''_5 - G'_5 G''_3}{2N} f_{11}, \tag{A3}$$

$$f_{14} = -\xi_0 H'_3 \int \frac{\eta G_3(\eta)}{(\xi_0^2 - \eta^2)^2} d\eta + \frac{H''_3}{2} f_{11}, \tag{A4}$$

$$f_{15} = \xi_0 H'_3 \int \frac{\eta G_3(\eta)}{(\xi_0^2 - \eta^2)^2} d\eta - \frac{(G_3 G''_5 - G_5 G''_3) H'_3}{2N} f_{11}. \tag{A5}$$

Furthermore, the functions $f_{21}(\xi_0)$ – $f_{26}(\xi_0)$ are given by

$$f_{21} = \frac{\xi_0^2}{2} \int \frac{(3\eta^2 - 1)(\eta^2 - 1)}{\xi_0^2 - \eta^2} d\eta, \tag{A6}$$

$$f_{22} = -H'_3 \int \frac{(1 - 3\eta^2)(2\eta^4 + \xi_0^2 - 3\xi_0^2 \eta^2)}{(\xi_0^2 - \eta^2)^2} d\eta + 3H_3 \xi_0 \int \frac{1 - 3\eta^2}{\xi_0^2 - \eta^2} d\eta, \tag{A7}$$

$$f_{23} = -\frac{49}{30N} G_3 H'_3 (1 - 3\xi_0^2) + H'_3 \int \frac{(1 - 3\eta^2)(2\eta^4 + \xi_0^2 - 3\xi_0^2 \eta^2)}{(\xi_0^2 - \eta^2)^2} d\eta, \tag{A8}$$

$$f_{24} = \frac{1}{c} \left[\xi_0 (\xi_0^2 - 1)^{1/2} \int \frac{(3\eta^2 - 1)}{(\xi_0^2 - \eta^2)^{3/2}} d\eta + \frac{\xi_0}{(\xi_0^2 - 1)^{1/2}} \int \frac{(3\eta^2 - 1)}{(\xi_0^2 - \eta^2)^{1/2}} d\eta \right], \tag{A9}$$

$$f_{25} = -\frac{\xi_0}{\xi_0^2 - 1} \int \frac{(1 - 3\eta^2)(2\xi_0^2 - \eta^2 - 1)G'_3(\eta)}{(\xi_0^2 - \eta^2)^2} d\eta + 3\xi_0 \int \frac{1 - 3\eta^2}{\xi_0^2 - \eta^2} d\eta - \frac{(\mu_r - 1)f_{12} + f_{13}}{\mu_r f_{14} + f_{15}} f_{22}, \tag{A10}$$

$$f_{26} = \frac{\xi_0}{\xi_0^2 - 1} \int \frac{(1 - 3\eta^2)(2\xi_0^2 - \eta^2 - 1)G'_3(\eta)}{(\xi_0^2 - \eta^2)^2} d\eta - \frac{49}{30N} (1 - 3\xi_0^2) G'_3 - \frac{(\mu_r - 1)f_{12} + f_{13}}{\mu_r f_{14} + f_{15}} f_{22}, \tag{A11}$$

$$f_\kappa = \frac{-72 + 106\xi_0^2 - 225\xi_0^4 + 135\xi_0^6 + 45\xi_0^4 (4 - 3\xi_0^2) \sqrt{\xi_0^2 - 1} \operatorname{arccsc}(\xi_0)}{15c^3 \xi_0^3 (\xi_0^2 - 1)^2}. \tag{A12}$$

The functions $f_{11}(\lambda_0)$ – $f_{15}(\lambda_0)$ are given by

$$f_{11} = \int \frac{\eta G_3(\eta)}{\lambda_0^2 + \eta^2} d\eta, \tag{A13}$$

$$f_{12} = \frac{1}{\lambda_0^2 + 1} \int G_3(\eta) \left(\frac{-2\eta G'_3(\eta)}{(\lambda_0^2 + \eta^2)^2} + \frac{G''_3(\eta)}{\lambda_0^2 + \eta^2} \right) d\eta, \tag{A14}$$

$$f_{13} = \frac{G'_3 G''_5 - G'_5 G''_3}{2N} f_{11}, \tag{A15}$$

$$f_{14} = \lambda_0 H_3' \int \frac{\eta G_3(\eta)}{(\lambda_0^2 + \eta^2)^2} d\eta - \frac{H_3''}{2} f_{11}, \quad (\text{A16})$$

$$f_{15} = -\lambda_0 H_3' \int \frac{\eta G_3(\eta)}{(\lambda_0^2 + \eta^2)^2} d\eta + \frac{(G_3 G_5'' - G_5 G_3'') H_3'}{2N} f_{11}. \quad (\text{A17})$$

Furthermore, the functions $f_{21}(\lambda_0)$ – $f_{26}(\lambda_0)$ are given by

$$f_{21} = \frac{\lambda_0^2}{2} \int \frac{(3\eta^2 - 1)(\eta^2 - 1)}{\lambda_0^2 + \eta^2} d\eta, \quad (\text{A18})$$

$$f_{22} = H_3' \int \frac{(3\eta^2 - 1)(\lambda_0^2 - 3\lambda_0^2 \eta^2 - 2\eta^4)}{(\lambda_0^2 + \eta^2)^2} d\eta + 3\lambda H_3 \int \frac{3\eta^2 - 1}{\lambda_0^2 + \eta^2} d\eta, \quad (\text{A19})$$

$$f_{23} = -H_3' \int \frac{(3\eta^2 - 1)(\lambda_0^2 - 3\lambda_0^2 \eta^2 - 2\eta^4)}{(\lambda_0^2 + \eta^2)^2} d\eta + \frac{49}{30N} (1 + 3\lambda_0^2) g_3 H_3', \quad (\text{A20})$$

$$f_{24} = \frac{1}{c} \left[\lambda_0 (\lambda_0^2 + 1)^{1/2} \int \frac{(1 - 3\eta^2)}{(\lambda_0^2 + \eta^2)^{3/2}} d\eta + \frac{\lambda_0}{(\lambda_0^2 + 1)^{1/2}} \int \frac{(1 - 3\eta^2)}{(\lambda_0^2 + \eta^2)^{1/2}} d\eta \right], \quad (\text{A21})$$

$$f_{25} = \frac{\lambda_0}{\lambda_0^2 + 1} \int \frac{(3\eta^2 - 1)(2\lambda_0^2 + \eta^2 + 1) G_3'(\eta)}{(\lambda_0^2 + \eta^2)^2} d\eta + 3\lambda \int \frac{3\eta^2 - 1}{\lambda_0^2 + \eta^2} d\eta + \frac{(\mu_r - 1) f_{12} + f_{13}}{\mu_r f_{14} + f_{15}} f_{22}, \quad (\text{A22})$$

$$f_{26} = -\frac{\lambda_0}{\lambda_0^2 + 1} \int \frac{(3\eta^2 - 1)(2\lambda_0^2 + \eta^2 + 1) G_3'(\eta)}{(\lambda_0^2 + \eta^2)^2} d\eta + \frac{49}{30N} (1 + 3\lambda_0^2) g_3' + \frac{(\mu_r - 1) f_{12} + f_{13}}{\mu_r f_{14} + f_{15}} f_{23}, \quad (\text{A23})$$

$$f_\kappa = \frac{72 + 106\lambda_0^2 + 225\lambda_0^4 + 135\lambda_0^6 - 45\lambda_0^4(4 + 3\lambda_0^2)\sqrt{\lambda_0^2 + 1} \operatorname{arccoth}(\sqrt{\lambda_0^2 + 1})}{15c^3 \lambda_0^3 (\lambda_0^2 + 1)^2}. \quad (\text{A24})$$

APPENDIX B: TRANSMEMBRANE POTENTIAL

The electric potential coefficients β_e , α_m , β_m , and α_i are obtained from the boundary conditions at $\xi = \xi_e$ and $\xi = \xi_i$ (see Fig. 1):

(a) Continuity of the potential:

$$\phi_e(\xi_e) = \phi_m(\xi_e), \quad \phi_m(\xi_i) = \phi_i(\xi_i). \quad (\text{B1})$$

(b) Continuity of the normal component of the complex current density, Eq. (9):

$$-\frac{K_e}{h_\xi} \frac{\partial \phi_e}{\partial \xi} \Big|_{\xi_e} = -\frac{K_m}{h_\xi} \frac{\partial \phi_m}{\partial \xi} \Big|_{\xi_e}, \quad -\frac{K_m}{h_\xi} \frac{\partial \phi_m}{\partial \xi} \Big|_{\xi_i} = -\frac{K_i}{h_\xi} \frac{\partial \phi_i}{\partial \xi} \Big|_{\xi_i}. \quad (\text{B2})$$

Condition (a) is justified because the normal component of the electric field must be bounded [25,33].

The remaining electric potential coefficients are given by

$$\alpha_i = \frac{c K_e K_m (\xi_i Q_i' - Q_i)(Q_e - \xi_e Q_e')}{D(\omega)}, \quad (\text{B3})$$

$$\alpha_m = \frac{c K_e (\xi_e Q_e' - Q_e)(K_i Q_i - K_m \xi_i Q_i')}{D(\omega)}, \quad (\text{B4})$$

$$\beta_m = \frac{c \xi_i K_e (K_i - K_m)(Q_e - \xi_e Q_e')}{D(\omega)}, \quad (\text{B5})$$

$$\beta_e = \frac{c \xi_i K_e (K_i - K_m) Q_e}{D(\omega)} + \frac{c \xi_e \{K_i (K_m - K_e) Q_i + K_m \xi_i [(K_m - K_i) Q_e' + (K_e - K_m) Q_i']\}}{D(\omega)}, \quad (\text{B6})$$

where

$$D(\omega) = K_e \xi_c Q'_e (-K_i Q_i + K_m \xi_i Q'_i) + Q_e [K_i K_m Q_i + (K_e - K_m)(K_i - K_m) \xi_i Q'_e - \xi_i Q'_i K_m^2], \quad (\text{B7})$$

and $Q_e \equiv Q_1(\xi_e)$, $Q_i \equiv Q_1(\xi_i)$, $Q'_e \equiv Q'_1(\xi_e)$, and $Q'_i \equiv Q'_1(\xi_i)$.

APPENDIX C: MAXWELL STRESSES

The Maxwell stresses in prolate coordinates are given by

$$\begin{aligned} \llbracket \mathbf{S}_{\xi\xi} \rrbracket &= \frac{1}{4c^2} \left\{ \frac{\eta^2 (\xi_0^2 - 1)}{\xi_0^2 - \eta^2} (c^2 - 2c\tau_3 Q'_1 + (\tau_3^2 + \tau_4^2)(Q'_1)^2) \right. \\ &\quad \left. + \frac{\xi_0^2 (\eta^2 - 1)}{\xi_0^2 - \eta^2} \left[c^2 - \frac{2c\tau_3 Q_1}{\xi_0} + (\tau_3^2 + \tau_4^2) \left(\frac{Q_1}{\xi_0} \right)^2 \right] - \frac{(\tau_1^2 + \tau_2^2)}{\epsilon_r} \left(\frac{\eta^2 (\xi_0^2 - 1)}{\xi_0^2 - \eta^2} + \frac{\xi_0^2 (\eta^2 - 1)}{\xi_0^2 - \eta^2} \right) \right\} \end{aligned} \quad (\text{C1})$$

and

$$\llbracket \mathbf{S}_{\xi\eta} \rrbracket = \frac{\eta}{2c^2} \frac{\sqrt{(\xi_0^2 - 1)(1 - \eta^2)}}{\xi_0^2 - \eta^2} \{ [c^2 \xi_0 - c(Q_1 + \xi_0 Q'_1) \tau_3 + (\tau_3^2 + \tau_4^2) Q_1 Q'_1] - (\tau_1^2 + \tau_2^2) \xi_0 / \epsilon_r \}, \quad (\text{C2})$$

where $\tau_1 = \text{Re}[\beta]$, $\tau_2 = \text{Im}[\beta]$, $\tau_3 = \text{Re}[\alpha]$, and $\tau_4 = \text{Im}[\alpha]$. Re and Im denote the real and imaginary parts.

The equivalent equations in the oblate coordinates are

$$\begin{aligned} \llbracket \mathbf{S}_{\lambda\lambda} \rrbracket &= \frac{1}{4c^2} \left\{ \frac{\eta^2 (\lambda_0^2 + 1)}{\lambda_0^2 + \eta^2} (c^2 - 2c\tau_3 Q'_1 + (\tau_3^2 + \tau_4^2)(Q'_1)^2) + \frac{\lambda_0^2 (\eta^2 - 1)}{\lambda_0^2 + \eta^2} \left[c^2 - \frac{2c\tau_3 Q_1}{\lambda_0} + (\tau_3^2 + \tau_4^2) \left(\frac{Q_1}{\lambda_0} \right)^2 \right] \right. \\ &\quad \left. - \frac{(\tau_1^2 + \tau_2^2)}{\epsilon_r} \left(\frac{\eta^2 (\lambda_0^2 + 1)}{\lambda_0^2 + \eta^2} + \frac{\lambda_0^2 (\eta^2 - 1)}{\lambda_0^2 + \eta^2} \right) \right\} \end{aligned} \quad (\text{C3})$$

and

$$\llbracket \mathbf{S}_{\lambda\eta} \rrbracket = \frac{\eta}{2c^2} \frac{\sqrt{(\lambda_0^2 + 1)(1 - \eta^2)}}{\lambda_0^2 + \eta^2} \{ [c^2 \lambda_0 - c(Q_1 + \lambda_0 Q'_1) \tau_3 + (\tau_3^2 + \tau_4^2) Q_1 Q'_1] - (\tau_1^2 + \tau_2^2) \lambda_0 / \epsilon_r \}. \quad (\text{C4})$$

APPENDIX D: ASYMPTOTIC ANALYSIS

$$A = (2 + \sigma_r)^2 + 9\omega^2, \quad (\text{D1})$$

$$B = 2\sigma_r^2(2 + \sigma_r)^2 + [18\sigma_r^2 + C_m^2(\sigma_r - 1)(2 + \sigma_r)^2(5 + 2\sigma_r) + 2C_m\sigma_r(\sigma_r + \sigma_r^2 - 2)]\omega^2, \quad (\text{D2})$$

$$C = -2\sigma_r^2(2 + \sigma_r)^3 [9 \text{Ca}_E(19 + 13\sigma_r) + 560(2 + \sigma_r)(4 + s_0)] - 71680C_m^2\omega^2 \quad (\text{D3})$$

$$\begin{aligned} &+ (9 \text{Ca}_E(2 + \sigma_r)[-6\sigma_r^2(121 + 71\sigma_r) + C_m(\sigma_r - 1)\sigma_r(2 + \sigma_r)(130 + 107\sigma_r) + C_m^2(60 + 23\sigma_r)(\sigma_r + \sigma_r^2 - 2)^2] \\ &+ 280(-72\sigma_r^2(2 + \sigma_r)^2(4 + s_0) + C_m^2(-64s_0 - \sigma_r(4 + \sigma_r)[4 + \sigma_r(2 + \sigma_r)][12 + \sigma_r(6 + \sigma_r)](4 + s_0)))\omega^2 \\ &- 9(-711 \text{Ca}_E C_m \sigma_r (\sigma_r + \sigma_r^2 - 2) + 288\sigma_r^2 [6 \text{Ca}_E + 35(4 + s_0)] + 5C_m^2(2 + \sigma_r)^2 [9 \text{Ca}_E (\sigma_r - 1)^2 \\ &+ 112(2 + \sigma_r)^2(4 + s_0)])\omega^4 - 22680C_m^2(2 + \sigma_r)^2(4 + s_0)\omega^6, \end{aligned}$$

$$G = 3 \text{Ca}_E [(2 + \sigma_r)^2 + 9\omega^2] (2\sigma_r^2(2 + \sigma_r)^2 + [18\sigma_r^2 + C_m^2(\sigma_r - 1)(2 + \sigma_r)^2(5 + 2\sigma_r) + 2C_m\sigma_r(\sigma_r + \sigma_r^2 - 2)]\omega^2). \quad (\text{D4})$$

-
- [1] J. L. Griffin, *Exp. Cell Res.* **61**, 113 (1970).
[2] F. J. Iglesias, M. C. Lopes, C. Santamaria, and A. Domingues, *Biophys. J.* **48**, 712 (1985).
[3] F. J. Asencor, C. Santamaria, F. J. Iglesias, and A. Dominguez, *Biophys. J.* **64**, 1626 (1993).
[4] A. W. Friend, Jr., E. D. Finch, and H. P. Schwan, *Science* **187**, 357 (1975).
[5] H. Engelhardt, H. Gaub, and E. Sackman, *Nature (London)* **307**, 378 (1984).
[6] M. Suga, T. Hatakeyama, and M. Isobe, *Jpn. J. Appl. Phys.* **36**, 396 (1997).
[7] K. A. Riske and R. Dimova, *Biophys. J.* **88**, 1143 (2005).
[8] K. A. Riske and R. Dimova, *Biophys. J.* **91**, 1778 (2006).
[9] R. Dimova, K. A. Riske, S. Aranda, N. Bezlyepkina, R. L. Knorr, and R. Lipowsky, *Soft Matter* **3**, 817 (2007).
[10] S. Aranda, K. A. Riske, R. Lipowsky, and R. Dimova, *Biophys. J.: Biophys. Lett.* **95**, L19 (2008).

- [11] E. Neumann, A. E. Sowers, and C. A. Jordan, *Electroporation and Electrofusion in Cell Biology* (Plenum, New York, 1989).
- [12] D. C. Chang, B. M. Chassey, J. A. Saunders, and A. E. Sowers, *Guide to Electroporation and Electrofusion* (Academic, New York, 1992).
- [13] U. Zimmermann and G. A. Neil, *Electromanipulation of Cells* (CRC, Boca Raton, FL, 1996).
- [14] W. Sung and P. J. Park, *Biophys. J.* **73**, 1797 (1997).
- [15] J. C. Neu and W. Krassowska, *Phys. Rev. E* **59**, 3471 (1999).
- [16] K. C. Smith, J. C. Neu, and W. Krassowska, *Biophys. J.* **86**, 2813 (2004).
- [17] W. Krassowska and P. D. Filev, *Biophys. J.* **92**, 404 (2011).
- [18] J. Teissié, J. M. Escoffre, M. P. Rols, and M. Golzio, *Radiol. Oncol.* **42**, 196 (2008).
- [19] T. Portet, C. Mauroy, V. Démercy, T. Houles, J.-M. Escoffre, D. S. Dean, and M.-P. Rols, *J. Membr. Biol.* **245**, 555 (2012).
- [20] P. F. Salipante, R. Knorr, R. Dimova, and P. M. Vlahovska, *Soft Matter* **8**, 3810 (2012).
- [21] W. Helfrich, *Z. Naturforsch.* **29c**, 182 (1974).
- [22] M. Winterhalter and W. Helfrich, *J. Coll. Int. Sci.* **122**, 583 (1988).
- [23] P. Peterlin, *J. Biol. Phys.* **36**, 339 (2010).
- [24] T. Yamamoto, S. Aranda-Espinoza, R. Dimova, and R. Lipowsky, *Langmuir* **26**, 12390 (2010).
- [25] H. Hyuga, K. Kinosita, Jr., and N. Wakabayashi, *Jpn. J. Appl. Phys.* **30**, 2649 (1991).
- [26] H. Hyuga, K. Kinosita, Jr., and N. Wakabayashi, *Jpn. J. Appl. Phys.* **30**, 1141 (1991).
- [27] M. M. Sadik, J. Li, J. W. Shan, D. I. Shreiber, and H. Lin, *Phys. Rev. E* **83**, 066316 (2011).
- [28] P. M. Vlahovska, R. S. Graciá, S. Aranda-Espinoza, and R. Dimova, *Biophys. J.* **96**, 4789 (2009).
- [29] J. Zhang, J. D. Zahn, W. Tan, and H. Lin, *Phys. Fluids* **25**, 071903 (2013).
- [30] M. Kummrow and W. Helfrich, *Phys. Rev. A* **44**, 8356 (1991).
- [31] P. Marszalek, D.-S. Liu, and T. Y. Tsong, *Biophys. J.* **58**, 1053 (1990).
- [32] I. Turcu and C. M. Lucaciu, *J. Phys. A* **22**, 985 (1989).
- [33] C. Grosse and H. P. Schwan, *Biophys. J.* **63**, 1632 (1992).
- [34] K. A. DeBruin and W. Krassowska, *Biophys. J.* **77**, 1213 (1999).
- [35] K. Maswiwat, D. Wachner, R. Warnke, and J. Gimsa, *J. Phys. D* **40**, 914 (2007).
- [36] G. Bryant and J. Wolfe, *J. Membr. Biol.* **96**, 129 (2008).
- [37] R. A. Jerry, A. S. Popel, and W. E. Brownell, *IEEE Trans. Biomed. Eng.* **43**, 970 (1996).
- [38] M. Klee and R. Plonsey, *Biophys. J.* **12**, 1661 (1972).
- [39] J. Gimsa and D. Wachner, *Biophys. J.* **77**, 1316 (1999).
- [40] K. Maswiwat, D. Wachner, and J. Gimsa, *Bioelectrochemistry* **74**, 130 (2008).
- [41] T. Kotnik and D. Miklavčič, *Biophys. J.* **79**, 670 (2000).
- [42] N. Benteñitis and S. Krause, *Langmuir* **21**, 6194 (2005).
- [43] J. Zhang, J. D. Zahn, and H. Lin, *Phys. Rev. E* **87**, 043008 (2013).
- [44] H. Nganguia, Y.-N. Young, P. M. Vlahovska, J. Bławdziewicz, J. Zhang, and H. Lin, *Phys. Fluids* **25**, 092106 (2013).
- [45] X. Wang, X.-B. Wang, and P. R. C. Gascoyne, *J. Electrostatics* **39**, 277 (1997).
- [46] G. Dassios, M. Hadjinicolaou, and A. C. Payatakes, *Quat. Appl. Math.* **52**, 157 (1994).
- [47] G. Dassios, M. Hadjinicolaou, F. A. Coutelieres, and A. C. Payatakes, *Int. J. Eng. Sci.* **33**, 1465 (1995).
- [48] S. Chandrasekhar, *Hydrodynamic and Hydromagnetic Stability* (Dover, New York, 1981).
- [49] R. M. Servuss, V. Harbich, and W. Helfrich, *Biochem. Biophys. Acta* **436**, 900 (1976).
- [50] G. Popescu, T. Ikeda, K. Goda, C. A. Best-Popescu, M. Laposata, S. Manley, R. R. Dasari, K. Badizadegan, and M. S. Feld, *Phys. Rev. Lett.* **97**, 218101 (2006).
- [51] M. D. Mitov, P. Méléard, M. Winterhalter, M. I. Angelova, and P. Bothorel, *Phys. Rev. E* **48**, 628 (1993).
- [52] P. Peterlin, S. Svetina, and B. Zeks, *J. Phys. Condens. Matter* **19**, 136220 (2007).
- [53] K. Antonova, V. Vitkova, and M. D. Mitov, *Europhys. Lett.* **89**, 38004 (2010).
- [54] J. T. Schwalbe, P. M. Vlahovska, and M. J. Miksis, *Phys. Rev. E* **83**, 046309 (2011).
- [55] J. Seiwert and P. M. Vlahovska, *Phys. Rev. E* **87**, 022713 (2013).
- [56] Y.-N. Young, S. Veerapaneni, and M. Miksis, (unpublished).
- [57] D. Lacoste, G. Menon, M. Z. Bazan, and J. F. Joanny, *Eur. Phys. J. E* **28**, 243 (2009).